Optimized Power System Voltage Measurements Considering Power System Harmonic Effects

Chukwuemeka Obikwelu(✉) and Sakis Meliopoulos

Electrical and Computer Engineering, Georgia Institute of Technology, Atlanta, GA 30332, USA
{cobikwelu3,sakis.m}@gatech.edu

Abstract. The paper presents a real-time error correction method that accurately estimates the primary quantity of an inductive instrument transformer – that is, a voltage or current transformer – based on a Dynamic-State-Estimation (DSE) optimization approach.

The DSE error-correction method uses a high-fidelity model of the voltage transformer (VT) instrumentation channel (IC) and the Unconstrained-Weighted-Least-Squares (UWLS) optimization approach to accurately estimate the VT primary voltage; thus, correcting for errors generated in the instrumentation channel. Specifically, the method involves obtaining discretized measurements of the VT load voltage through a continuous monitoring process. The VT primary voltage is then continuously estimated by the method based on fitting the continuously obtained measurement samples to the high-fidelity VT model. The continuously estimated primary voltage can then be made readily available for metering, protection, and control functions. The method can be implemented using microprocessor technology, for example, in Merging Unit (MU) applications for digital power substation architectures.

The paper will focus on evaluating the performance of the DSE-based error-correction method, applied to inductive voltage transformer instrumentation channel (VTIC) applications, in the estimation of primary voltage signals distorted by harmonics. The evaluation process will employ multiple Fourier analysis techniques.

Keywords: VT · DFT · DSE · Optimization

1 Introduction

Harmonics in power systems are generally caused by nonlinear loading and device operations that draw non-sinusoidal currents from sinusoidal voltage sources – resulting in the injection of parasitic harmonic power into the power system, causing power quality problems. Harmonics circulation occurs primarily in distribution power systems. This is due to the nonlinear loads that are directly interconnected to distribution systems – e.g., industrial loads, and distributed generation (DG). Furthermore, with increasing DG connections, the number of inverter-based technologies is also increasing. The power electronics associated with these technologies can generate various harmonics

J. L. Afonso et al. (Eds.): SESC 2020, LNICST 375, pp. 152–171, 2021.
https://doi.org/10.1007/978-3-030-73585-2_10

in distribution systems. Other sources of harmonics include electric machine energization events, and operating transformers or electric machines in the nonlinear regions of their excitation-characteristics during stressed power system conditions. While transient events, such as equipment energization, can introduce harmonics onto the power system, harmonic effects are generally classified as steady-state phenomena. It is thus important to monitor power system harmonic levels as a prerequisite for and in support of implementing power quality improvement strategies. The VT is indispensably essential to this monitoring process.

Voltage transformers (VTs) provide scaled down replicas of the system-level voltage to low-voltage instrumentation devices. For example, typical VT secondary voltages used in protective relaying are 66.4 V, 115 V, and 120 V. The "instrumentation channel" delivers the scaled replica voltage to the connected devices, where it can then be used for metering, protection, and/or control schemes. The conventional or inductive voltage transformer instrumentation channel (VTIC) comprises the instrument transformer core, primary and secondary windings, control cables, electric loads, filters, and A/D converters. It is essential that the VTIC delivers accurate representations of the power system voltage to the connected devices during normal and disturbed system operations, otherwise the associated protection, control and/or monitoring functions may be compromised – posing risks to the power system.

Except for the scaling down, the replica or reproduced voltage should ideally resemble the primary voltage – in terms of waveshape, frequency, phase-shift, and harmonic content. However, instrumentation channel limitations and dynamics may cause the reproduced voltage to deviate from the ideal, and thus not represent a perfect replica of the primary voltage.

It is important to note that the transfer function of the VT behaves like a low-pass filter, causing higher harmonic signal components to experience varying degrees of attenuation. Furthermore, when harmonic content frequencies match any of the natural frequencies of the instrumentation channel, resonance effects (characterized by harmonic voltage swells) may significantly distort the secondary voltage. The resonance effects are caused by interactions within the VTIC, between the leakage inductances, magnetizing branch inductance and parasitic capacitances, in response to the harmonic content of the driving input or primary voltage. Therefore, the attenuation or swelling of harmonic voltage signal components may cause secondary voltage distortions, such that the secondary voltage no longer accurately represents a scaled-down replica of the primary voltage. More specifically, the harmonic content of the secondary voltage may no longer adequately represent the harmonic content of the primary voltage due to instrumentation channel limitations – thus, signifying the generation of channel errors. The inability of the VT to accurately reproduce the harmonic content present in primary voltage and thus present in the power system can be problematic for power quality monitoring.

The earlier mentioned instrumentation channel dynamics, which can contribute to the generation of error effects within the channel, generally refer to interactions between power system factors and instrumentation channel factors. These interactions are exacerbated by the limitations of the instrumentation channel, such as magnetic core size, etc. Examples of related power system factors are high source X/R ratio, system topography,

and harmonics; examples of related VTIC factors are magnetic core characteristics, burden level, parasitic capacitances, leakage inductances and ferro-resonance suppression circuit parameters. The generated channel error effects include: magnetic core saturation; harmonic distortions in the secondary signal; transient secondary waveform irregularities, as occurs in Coupled-Capacitor-VT (CCVT) applications – where the discharging of CCVT internal energies, after fault-related system voltage collapse, results in nontrivial transient secondary waveform distortions.

It is therefore valuable to develop online methods that reliably correct for VTIC errors, which cause inaccuracies in both the fundamental and harmonic components of the secondary voltage measurement. The method studied in this paper is intended to achieve this online correction and provide optimized power system voltage measurements for connected secondary subsystem functions. Earlier related work is covered in [4] and the application of the method for current transformer instrumentation channel (CTIC) error correction is covered in [5] and [12].

2 Literature Review

Historically, different methods have been applied to correct for instrument transformer instrumentation channel (ITIC) error generation, although many of these methods focus on error-correction for current transformers (CTs). The method in [1] provides compensation for CCVTIC transient errors based on the digital inversion of the CCVT transfer function. This approach does not use a detailed CCVT model, is highly vulnerable to resonance effects, and neglects saturation possibilities. [2] proposes an output tracking VTIC error-correction method, based on repetitive learning control, for reproducing the primary voltage. The performance of the method may be jeopardized by serious saturation effects and the poor selection of controller gains. [3] proposes a CCVT error-correction method that estimates the primary voltage based on nonlinear least-squares fitting. The method may be vulnerable to convergence problems (from poor state vector initialization), and to errors from saturation effects and system harmonics unaccounted for in its fitting model. None of the reviewed methods were applied in cases where the primary voltage (to be reconstructed or estimated) is corrupted with harmonics – thus, how they would perform in such cases is uncertain. Furthermore, the reviewed methods may be suitable for control functions but not for protective relaying since their respective algorithms are not structured for real-time implementation.

This paper presents a new method for estimating the VT primary voltage on a sample-by-sample basis, using continuously obtained sample measurements of the VT load voltage. The method involves modeling the VTIC in detail and applying the unconstrained weighted least-squares (UWLS) dynamic state estimation (DSE) method to accurately estimate the primary voltage. The method is designed for real-time implementation, performs robustly with noisy inputs, and is immune to remnant flux effects. The paper will focus on evaluating the performance of the method in cases where the primary voltage is corrupted with harmonic components.

3 Methodology

The methodology involves a series of model development steps leading up to the formulation of the estimation problem. Different Least-Squares methods can be applied to solve the problem, but the presented methodology uses the Unconstrained Weighted Least-Squares (UWLS) technique.

3.1 VT Instrumentation Channel Electrical Circuit Model

The device or system under study, that is, the instrumentation channel, is first represented by a detailed electrical circuit. The circuit is parametrized to account for the unknown state variables. The device is then mathematically modeled by a system of algebraic, nonlinear, and differential equations, expressed in terms of the state variables. The system of equations is generally derived based on: applying Kirchhoff's Current and Voltage Laws at the nodes and within the loops of the electrical circuit model, respectively; applying Faraday's Law of Induction to relate the internal voltage with the flux; and, applying a high-order equation to model the nonlinear relationship between the magnetizing current and the flux.

Figure 1 shows the non-ideal or detailed high-frequency VTIC circuit model, including parasitic capacitances (C_1, C_2, C_3 and C_4). For the study, the following simplifications are made to the provided electrical circuit model:

1. The magnetizing branch current becomes insignificant in the high-frequency range. Coupling the latter point with the assumption that the VT is operating within the linear region of its excitation curve, the magnetizing branch may be neglected without consequences.
2. In the high-frequency range, it is necessary to model the transformer leakage reactances. But the parasitic capacitances may be neglected unless their effects have been found to be significant. Thus, there are generally two high-frequency range models, both including the transformer leakage reactances – one with parasitic capacitances and one without them. It may be important to model the parasitic capacitances depending on the harmonic effects being considered. For this study, the resonance effects of the parasitic capacitances are negligible for the range of harmonics considered – therefore, the capacitances are neglected.

The resulting circuit model is thus a high-frequency model, neglecting parasitic capacitance effects. The system of nonlinear, algebraic, and differential equations formed from the circuit model in Fig. 1 comprises 19 equations and 19 unknowns or state variables [4]. The above simplifications to the circuit model result in a system of algebraic and differential equations, comprising 11 equations and 11 state variables. The state vector is shown in (1), representing the minimum number of states that can be applied to fully describe the circuit model.

$$\mathbf{x}_1 = [\,v_1(t)\;\; v_2(t)\;\; v_3(t)\;\; v_4(t)\;\; v_5(t)\;\; v_6(t)\;\; e_C(t)\;\; i_{L1}(t)\;\; i_{L2}(t)\;\; i_{L3}(t)\;\; i_{L4}(t)\,]^T \quad (1)$$

The voltages and currents in (1) are shown in Fig. 1. Note that the intended connection for the VT in this analysis is between phase and ground, and thus node 2 in Fig. 1

is grounded. Figure 2 presents the system of algebraic and differential equations that mathematically describes the VTIC circuit model shown in Fig. 1, after simplification. The stabilizing conductances (i.e., g_{s1}, g_{s2}, g_{s3} and g_{s4}), which are connected in-parallel with the circuit inductances, are not included in Fig. 1 for simplification purposes – but they are accounted for in the system of equations shown in Fig. 2. Furthermore, g_B represents the load conductance, and M_{34} represents the mutual inductance of the two-way secondary cabling.

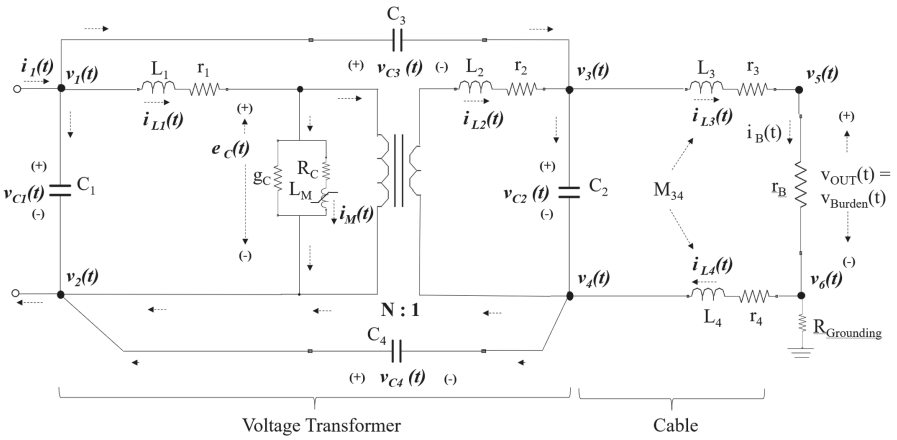

Fig. 1. High-frequency, non-ideal VTIC electrical circuit model, featuring parasitic capacitances.

The quadratization of the circuit model, as performed in related work in [4] and [5], is not needed in this analysis due to the applied simplifications. More specifically, the reasonable assumption of linear device operation and neglecting the magnetizing branch due to analysis in the high-frequency range remove the equations for modeling nonlinear excitation behavior from the mathematical model. Therefore, the next step is to use the mathematical model provided in Fig. 2 to develop the dynamic measurement models.

3.2 VT Instrumentation Channel Measurement Models

Dynamic Measurement Model (DMM)

The DMM framework mathematically associates the obtained measurements with the theoretical system model, plus error, as shown in (2).

$$\mathbf{z}(t) = \mathbf{h}(\mathbf{x}(t)) + \boldsymbol{\eta} \tag{2}$$

$$
\begin{aligned}
1.\quad & 0 = -\{v_1(t) - v_2(t)\} + r_1 \cdot \left\{ i_{L1}(t) + g_{s1} L_1 \frac{di_{L1}(t)}{dt} \right\} + L_1 \frac{di_{L1}(t)}{dt} + e_c(t) \\
2.\quad & 0 = -\frac{e_c(t)}{N} + L_2 \frac{di_{L2}(t)}{dt} + r_2 \cdot \left\{ i_{L2}(t) + g_{s2} L_2 \frac{di_{L2}(t)}{dt} \right\} + \{v_3(t) - v_4(t)\} \\
3.\quad & 0 = -\{v_6(t) - v_4(t)\} + r_4 \cdot \left\{ i_{L4}(t) + g_{s4} \{L_4 \frac{di_{L4}(t)}{dt} - M_{34} \frac{di_{L3}(t)}{dt}\} \right\} + \left\{ L_4 \frac{di_{L4}(t)}{dt} - M_{34} \frac{di_{L3}(t)}{dt} \right\} \\
4.\quad & 0 = -\{v_3(t) - v_5(t)\} + r_3 \cdot \left\{ i_{L3}(t) + g_{s3} \{L_3 \frac{di_{L3}(t)}{dt} - M_{34} \frac{di_{L4}(t)}{dt}\} \right\} + \left\{ L_3 \frac{di_{L3}(t)}{dt} - M_{34} \frac{di_{L4}(t)}{dt} \right\} \\
5.\quad & v_{out}(t) = v_5(t) - v_6(t) \\
6.\quad & 0 = N \cdot \left\{ i_{L1}(t) + g_{s1} L_1 \frac{di_{L1}(t)}{dt} \right\} - \left\{ i_{L2}(t) + g_{s2} L_2 \frac{di_{L2}(t)}{dt} \right\} \\
7.\quad & 0 = i_{L2}(t) + g_{s2} L_2 \frac{di_{L2}(t)}{dt} - \left\{ i_{L3}(t) + g_{s3} \{L_3 \frac{di_{L3}(t)}{dt} - M_{34} \frac{di_{L4}(t)}{dt}\} \right\} \\
8.\quad & 0 = i_{L3}(t) + g_{s3} \cdot \left\{ L_3 \frac{di_{L3}(t)}{dt} - M_{34} \frac{di_{L4}(t)}{dt} \right\} - g_B \{v_5(t) - v_6(t)\} \\
9.\quad & 0 = -\left\{ i_{L4}(t) + g_{s4} \cdot \left\{ L_4 \frac{di_{L4}(t)}{dt} - M_{34} \frac{di_{L3}(t)}{dt} \right\} \right\} + g_B \{v_5(t) - v_6(t)\} \\
10.\quad & 0 = -\left\{ i_{L2}(t) + g_{s2} L_2 \frac{di_{L2}(t)}{dt} \right\} + \left\{ i_{L4}(t) + g_{s4} \{L_4 \frac{di_{L4}(t)}{dt} - M_{34} \frac{di_{L3}(t)}{dt}\} \right\} \\
11.\quad & 0 = N \cdot \left\{ i_{L1}(t) + g_{s1} L_1 \frac{di_{L1}(t)}{dt} \right\} - g_B \{v_5(t) - v_6(t)\}
\end{aligned}
$$

Fig. 2. Mathematical model for the VTIC electric circuit model, after applying the proposed simplifications to the circuit in Fig. 1.

where **z**(t) is the measurement vector, comprising four different kinds of measurements to be discussed subsequently; **x**(t) is the state vector in (2); **h**(**x**(t)) is the overdetermined, theoretical system model, written in matrix equation form in (3); and, **η** is the error vector.

$$
\mathbf{h}(\,\mathbf{x}(t)\,) = \mathbf{Y}_{\mathbf{eq}} \cdot \mathbf{x}(t) + \mathbf{B}_{\mathbf{eq}} \cdot \frac{\mathrm{d}}{\mathrm{dt}} \{\,\mathbf{x}(t)\} + \begin{bmatrix} \mathbf{x}(t)^{\mathrm{T}} \cdot \mathbf{F}_{\mathbf{eq1(S\times S)}} \cdot \mathbf{x}(t) \\ \vdots \\ \mathbf{x}(t)^{\mathrm{T}} \cdot \mathbf{F}_{\mathbf{eqN_m(S\times S)}} \cdot \mathbf{x}(t) \end{bmatrix} + \mathbf{C}_{\mathbf{eq}} \qquad \text{Quadratic Terms} \tag{3}
$$

where $\mathbf{Y}_{\mathrm{eq}}$, $\mathbf{B}_{\mathrm{eq}}$, $\mathbf{F}_{\mathrm{eq(1\text{-}Nm)}}$ and $\mathbf{C}_{\mathrm{eq}}$ are the coefficient matrices of the linear, differential, *quadratic* and constant parts, respectively; S is the number of states after quadratization; N_m is the number of elements in the measurement vector. Quadratic terms, and additional state variables, typically result from the quadratization process. But due to the applied simplifications, the measurement model does not have any quadratic terms; thus, the matrix formulation accounting for them in (3) above can be neglected without consequence. The overdetermined system model used in the DMM framework (that is, the DMM system model) is shown in Fig. 3.

1. $0 = -\{v_1(t) - v_2(t)\} + r_1 \cdot \left\{ i_{L1}(t) + g_{s1} L_1 \frac{di_{L1}(t)}{dt} \right\} + L_1 \frac{di_{L1}(t)}{dt} + e_c(t)$
2. $0 = -\frac{e_c(t)}{N} + L_2 \frac{di_{L2}(t)}{dt} + r_2 \cdot \left\{ i_{L2}(t) + g_{s2} L_2 \frac{di_{L2}(t)}{dt} \right\} + \{v_3(t) - v_4(t)\}$
3. $0 = -\{v_6(t) - v_4(t)\} + r_4 \cdot \left\{ i_{L4}(t) + g_{s4} \{L_4 \frac{di_{L4}(t)}{dt} - M_{34} \frac{di_{L3}(t)}{dt}\} \right\} + \left\{ L_4 \frac{di_{L4}(t)}{dt} - M_{34} \frac{di_{L3}(t)}{dt} \right\}$
4. $0 = -\{v_3(t) - v_5(t)\} + r_3 \cdot \left\{ i_{L3}(t) + g_{s3} \{L_3 \frac{di_{L3}(t)}{dt} - M_{34} \frac{di_{L4}(t)}{dt}\} \right\} + \left\{ L_3 \frac{di_{L3}(t)}{dt} - M_{34} \frac{di_{L4}(t)}{dt} \right\}$
5. $v_{out}(t) = v_5(t) - v_6(t)$
6. $0 = N \cdot \left\{ i_{L1}(t) + g_{s1} L_1 \frac{di_{L1}(t)}{dt} \right\} - \left\{ i_{L2}(t) + g_{s2} L_2 \frac{di_{L2}(t)}{dt} \right\}$
7. $0 = i_{L2}(t) + g_{s2} L_2 \frac{di_{L2}(t)}{dt} - \left\{ i_{L3}(t) + g_{s3} \{L_3 \frac{di_{L3}(t)}{dt} - M_{34} \frac{di_{L4}(t)}{dt}\} \right\}$
8. $0 = i_{L3}(t) + g_{s3} \cdot \left\{ L_3 \frac{di_{L3}(t)}{dt} - M_{34} \frac{di_{L4}(t)}{dt} \right\} - g_B \{v_5(t) - v_6(t)\}$
9. $0 = -\left\{ i_{L4}(t) + g_{s4} \cdot \left\{ L_4 \frac{di_{L4}(t)}{dt} - M_{34} \frac{di_{L3}(t)}{dt} \right\} \right\} + g_B \{v_5(t) - v_6(t)\}$
10. $0 = -\left\{ i_{L2}(t) + g_{s2} L_2 \frac{di_{L2}(t)}{dt} \right\} + \left\{ i_{L4}(t) + g_{s4} \{L_4 \frac{di_{L4}(t)}{dt} - M_{34} \frac{di_{L3}(t)}{dt}\} \right\}$
11. $0 = N \cdot \left\{ i_{L1}(t) + g_{s1} L_1 \frac{di_{L1}(t)}{dt} \right\} - g_B \{v_5(t) - v_6(t)\}$
12. $i_B(t) = g_B \cdot \{v_5(t) - v_6(t)\}$
13. $i_B(t) = i_{L2}(t) + g_{s2} L_2 \frac{di_{L2}(t)}{dt}$
14. $i_B(t) = i_{L3}(t) + g_{s3} \cdot \left\{ L_3 \frac{di_{L3}(t)}{dt} - M_{34} \frac{di_{L4}(t)}{dt} \right\}$
15. $i_B(t) = i_{L4}(t) + g_{s4} \cdot \left\{ L_4 \frac{di_{L4}(t)}{dt} - M_{34} \frac{di_{L3}(t)}{dt} \right\}$
16. $0 = v_2(t)$
17. $0 = v_6(t)$

Fig. 3. VTIC dynamic measurement model (DMM) system model.

The measurement vector **z**(t) comprises four kinds of measurements, namely:

- Actual measurements: The only actual measurement in the DMM is the output or load voltage. Equation (5) in Fig. 3 represents the *actual* measurement.
- Virtual measurements: This serves to represent the implementation a physical law, such as Faraday's Induction Law, Kirchhoff's Current Law (KCL) or Kirchhoff's Voltage Law (KVL). Equations (1) through (4) and (6) through (11) in Fig. 3 represent *virtual* measurements.
- Derived measurements: This is a measurement that is derived from an actual measurement. The derived measurement shares the same error as the actual measurement used for its derivation. Equations (12) through (15) in Fig. 3 represent *derived* measurements.
- Pseudo measurements: This is a hypothetical measurement, where its expected value can be guessed although with high uncertainty. Equations (16) and (17) in Fig. 3 represent *pseudo* measurements.

Algebraic Companion Form (ACF) Measurement Model
The ACF measurement model results from integrating the DMM using the Quadratic Integration method [6], which is in the family of Lobatto-Runge-Kutta numerical integration methods. The quadratic integration method does two key things:

- The system model equations are integrated assuming that the system states vary quadratically within each time step.
- Reformulates the nonlinear system model equations as a fully equivalent system of quadratic algebraic equations (by introducing additional state variables).

The integration time-step h, also the DSE time-step, is set to twice the sampling period (Ts) of the streaming measurements. The DMM is then integrated from time $t - h$ to t_m (that is, $t - h/2$) and from time $t - h$ to t. Thus, the measurement vector $\mathbf{z}(t,tm)$ now contains two sets of measurements: the first set of measurements at time t, stacked on-top of a second set of the same measurements but at time t_m (or one sampling period prior). The system model $\mathbf{h}(\mathbf{x}(t,t_m))$ is now expressed as a function of an expanded state vector, $\mathbf{x}(t,t_m)$. The state vector $\mathbf{x}(t,t_m)$ now has two sets of state variables: the first set of states at time t, stacked on-top of the second set of states at time t_m (or one sampling period prior).

The ACF measurement model is the final state of the model development process. The next step is to apply this measurement model in the formulation and resolution of the estimation problem. Given the ACF measurement model setup, the error-correction algorithm is setup such that, at each DSE timestep, it provides the best-estimates least-squares state vector solution at the current time t and at time $t - h/2 = t - Ts$. This setup provides the basis for the specification of a criterion for real-time execution, which the proposed method adheres to. The criterion is stated as follows: for real-time execution, the algorithm should provide the estimates at times t and $t - h/2$ (i.e., the present time and one sampling period prior) before the arrival of the next sample, which is one DSE time-step (that is, two sampling periods) away.

3.3 Problem Formulation and Solution Method

Using the ACF measurement model, the estimation problem is formulated as an unconstrained weighted least squares (UWLS) optimization problem – as shown in (4) and (5).

$$\min\ J(x(t,t_m)) = \sum_{j=1}^{N_{mm}} \left(\frac{z^{(j)}(t,t_m) - h^{(j)}(x(t,t_m))}{\sigma^{(n)}} \right)^2 = \sum_{j=1}^{N_{mm}} \left(\frac{\eta^{(j)}}{\sigma^{(j)}} \right)^2 = \sum_{j=1}^{N_{mm}} \left(s^{(j)} \right)^2 \tag{4}$$

$$\min\ J = \boldsymbol{\eta}^T \cdot \mathbf{W} \cdot \boldsymbol{\eta} \tag{5}$$

where, $s^{(j)}$ represents the normalized residual for the j^{th} measurement; $\sigma^{(j)}$ represents the standard deviation of the meter measurement errors associated with the j^{th} measurement. In the compact vector form, $\boldsymbol{\eta}$ represents the $m \times 1$ vector of random

errors, where *m* represents the number of measurements in the expanded measurement vector; the weighting matrix *W* represents the diagonal matrix of the squared reciprocals of the standard deviation values, that is, $diag(\ (1/\ \sigma^{(j)})^2)$.

The solution to the weighted least squares optimization problem in (4) is obtained using the Gauss-Newton iterative algorithm [7, 8], shown in (6) below.

$$\mathbf{x}^{v+1}(t, t_m) \ = \ \mathbf{x}^{v}(t, t_m) + (\mathbf{H}^T \cdot \mathbf{W} \cdot \mathbf{H})^{-1} \cdot \mathbf{H}^T \cdot \mathbf{W} \cdot \left(\mathbf{z}(t, t_m) - \mathbf{h}(\ \mathbf{x}^{v}(t, t_m)\ )\right) \quad (6)$$

In (6), *v* represents the iteration number, and the algorithm iterates until a predefined resolution ε is attained, i.e., $|\boldsymbol{x}^{v+1} - \boldsymbol{x}^{v}| < \boldsymbol{\varepsilon}$, at which time $\mathbf{x}^{v+1} = \hat{\mathbf{x}}(t, t_m)$ *or* $\hat{\mathbf{x}}$ - where $\hat{\mathbf{x}}$ represents the state vector of the best-estimate Least-Squares (LS) solution at times *t* and t_m; $\boldsymbol{H}$ represents the Jacobian of $\boldsymbol{h}(\hat{\mathbf{x}})$ or $\delta\, \mathbf{h}(\ \widehat{\mathbf{x}}(t, t_m)\ ) \Big/ \delta \mathbf{x}$ computed at each time-step. The main diagonal of the variance-covariance matrix in (6), that is $(\mathbf{H}^{\mathrm{T}} \cdot \mathbf{W} \cdot \mathbf{H})^{-1}$, provides the variances of the estimated states.

The final step involves the application of the Goodness-of-Fit (GOF) method to mathematically assess how well or *confidently* the model (using the best-estimates least-squares state vector solution to update the state variables) fits the measurements. A high confidence level means the model matches the measurements; a low confidence level indicates the presence of measurement or modeling errors. The mathematical formulation of the GOF statement can be found across [4, 5, 8] and [12].

4 Simulation Setup

4.1 Power System Setup

WinIGS [10] is used to model the system and generate the simulation use-cases. The software also generates the COMTRADE files that are used in a MATLAB script to perform the estimation calculations. The simulated power system single-line diagram is shown in Fig. 4. The main three-phase generator is specified at 13 kV_{LL} and is a positive-sequence sinusoidal 60 Hz voltage source. Two three-phase generator sources are added in-parallel to the main generator to inject 9^{th} (15%) and 11^{th} (10%) order harmonics into the system. The 9^{th} and 11^{th} harmonics have magnitudes of 15% and 10% of the magnitude of the fundamental component, respectively. The phase angles of the 9^{th} and 11^{th} harmonic components are both at zero degrees. The delta-wye (grounded) generator step-up (GSU) power transformer, specified at 14 kV_{LL}/125kV_{LL}, generates 116 kV_{LL} at the transmission system level. The VT is specified at $115/\sqrt{3}$ kV_{LN}:115V. The "LL" and "LN" subscripts denote "Line-to-Line" and "Line-to-Neutral," respectively.

It is worth noting that the 9^{th} or otherwise called *triplen* harmonic voltage generator source is applied across each winding of the GSU transformer and thus electromagnetically reproduced on the transmission system side; however, any harmonic generator-side triplen harmonic current ends up circulating within the delta-connected primary winding of the GSU transformer – not passing through, as it classifies as a zero-sequence current.

Therefore, the periodic and continuous-time signal *v(t)* at the *VT* primary features a *Total Harmonic Distortion* (THD) value as computed in (8), where the *Fourier Series* decomposition of *v(t)* is provided in (7).

$$v(t) = V_{average} + \sum_{n=1}^{9,11} V_n \cdot sin(n \cdot w_1 \cdot t + n \cdot \theta_n) \quad (7)$$

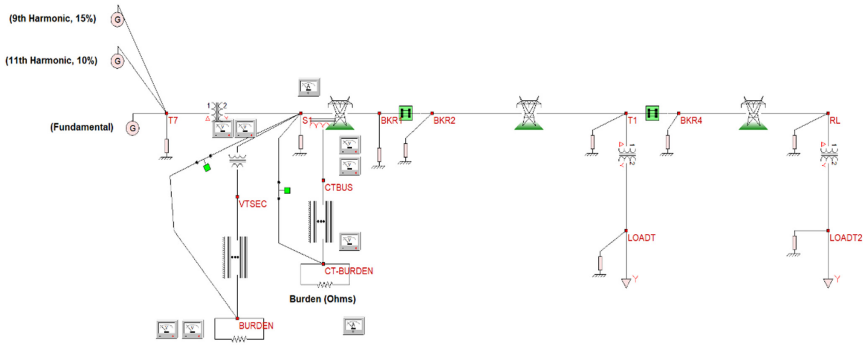

Fig. 4. The simulated test power system.

$$\text{THD}(\%) = \frac{\sqrt{IHC_2^2 + IHC_3^2 + \ldots + IHC_n^2}}{IHC_1} = \frac{\sqrt{IHC_9^2 + IHC_{11}^2}}{IHC_1} = \frac{\sqrt{\{0.15\}^2 + \{0.10\}^2}}{1} = 0.1803 \cong 18\% \tag{8}$$

where "IHC" means individual harmonic contribution; n indexes the harmonic contributions; V_n is the amplitude of the n^{th} harmonic; w_1 is the radian frequency of the first harmonic or the fundamental signal component; θ_n is the phase shift angle of the n^{th} harmonic, and $V_{average}$ represents any DC or constant term in the signal (typically equaling zero if no nonzero DC term is present).

Note that the energizations of the two power distribution transformers downstream in Fig. 4 inject even-harmonics (particularly second and/or fourth) into the power system. The prominence of each injected harmonic in the frequency spectrum will depend on its individual magnitude relative to that of the fundamental component.

4.2 Sampling Process, Simulation Parameters and Simulation Use-Case Scenarios

Sampling Process

The discrete-time (DT) signal is formed from periodically sampling the analog, continuous-time signal. The continuous-time signal is first operated on using the Shah function *III(x)* [9], modified by the desired sampling period (*Ts*), to form the first stage of the sampled signal – that is, a periodic sequence of impulses interspaced in time by *Ts*, where *fs* = *1/Ts* represents the sampling rate. The sampled signal is then converted from a sequence of impulses to one of sample values, or a discrete sequence, such that each sample in the sequence is located by an integer multiple of *Ts*. If v(t) is the continuous-time signal, then the periodic sequence of impulses is formed as follows in (9) and (10).

$$III(t) = \sum_{n=-\infty}^{\infty} \delta(t - n \cdot T_s) \tag{9}$$

$$v_s(t) = III(t) \cdot v(t) = \left\{\sum_{n=-\infty}^{\infty} \delta(t - n \cdot T_s)\right\} \cdot v(t) = \sum_{n=-\infty}^{\infty} v(n \cdot T_s) \cdot \delta(t - n \cdot T_s) \tag{10}$$

Using $v(n{\cdot}Ts)$ to abbreviate the sequence of impulses in (10) for the range of n integer indices, a one-to-one mapping process can then be used to convert the series of impulses into the discrete sequence of sample values $v[n]$ – thus, given $v(t)$,

$$v[n] = v(n \cdot T_s), \quad n \varepsilon Z \quad \text{(set of positive and negative integers, including 0)} \tag{11}$$

Simulation Parameters
The simulated signal sampling rate (f_s) is 80 samples/cycle, which is 4800 samples/second and represents a sampling period or time-interval (Ts) of 208.33 μsecs. The simulation duration is 500 milli-seconds, and thus there are 2400 samples in the discrete-time signal $v[n]$. The quadratic integration time-step (h), also called the DSE time-step, used in the algorithm is twice the sampling period (that is, 416.66 μs).

Simulation Use-Case Scenarios
The VT load is 50 Ω, and the instrumentation channel cable type is Cu-#10. The VT secondary burden comprises the cable leads and the connected load. Three simulations are conducted – the first at a cable length 0.01 miles (52.8 ft); the second at a cable length of 0.08 miles (422.4 ft), and the third at a cable length of 0.16 miles (844.8 ft). Reducing the load resistance and/or increasing the cable length increases the magnitude and phase errors generated in the instrumentation channel. In each simulation use-case, the VT primary and load voltages are measured.

5 Analysis Methods and Presentation of Results

The metered VT secondary voltage, referred to the primary side using the voltage transformation ratio (VTR) of the VT, serves as the uncorrected voltage reference. The metered system voltage serves as the actual primary or ratio voltage reference. The uncorrected voltage reference and the ratio voltage reference are compared to show the errors resulting from the instrumentation channel.

The estimated primary voltage is then compared against the ratio voltage reference to confirm and quantify the degree of error correction. The comparisons are conducted in the time, phasor, and frequency domains.

5.1 Time Domain Comparison Methods

Equation (12) is applied to plot the instantaneous differences between the actual and estimated primary voltages. The normalized-root-mean-square-error (NRMSE) formula, shown in (13), is used to evaluate the estimation residual between the actual and estimated VT primary voltages – where lower residuals indicate less estimation error. In both equations, note that $t = n{\cdot}Ts$ and n is the sample value index

$$\Delta v(t)_{PER\_UNIT} = \frac{v_p(t) - v_{p\_est}(t)}{v_p(t)} \tag{12}$$

$$\varepsilon_{NRMSE}\% = \frac{\sqrt{\frac{1}{N} \cdot \sum_{j=1}^{N} \left(v_p(j) - v_{p\_est}(j)\right)^2}}{\max(v_p) - \min(v_p)} \times 100 \tag{13}$$

where N represents the number of sample intervals; v_{p_est} represents the estimated VT primary voltage; v_p represents the actual VT primary voltage.

5.2 Phasor Domain Comparison Methods

The RMS magnitudes of the estimated and uncorrected signals are respectively compared against the RMS magnitude of the ratio voltage reference signal. The phase angles of the estimated and uncorrected signals are also respectively compared against the phase angles of the ratio voltage reference signal. The phase angle and RMS magnitude are derived from the computed phasor. The phasor may be computed over a full, half or quarter cycle. The full-cycle phasor computation approach is taken in this paper.

Generally, consider the ***Fourier series*** expansion of a cosine sinusoid (14) up to the m^{th} harmonic, and assuming a zero DC term.

$$v(t) = A_1 \cdot \cos(w \cdot t + \phi_1) + A_2 \cdot \cos(2 \cdot w \cdot t + \phi_2) + \ldots + A_m \cos(m \cdot w \cdot t + \phi_m) \tag{14}$$

where A_m is the maximum value of the m^{th} harmonic; w is the radian frequency and ϕ_m is the phase shift of the m^{th} harmonic. Focusing on the fundamental signal component, (14) can be resolved into (15), where a_1 and a_2 can then be applied in (16) and (17) to form the phasor ($\frac{A_1}{\sqrt{2}} \cdot e^{j\varnothing_1} = A_{1,RMS} \cdot e^{j\varnothing_1}$).

$$v(t_i) = \{a_1\} \cdot \cos(w \cdot t_i) - \{a_2\} \cdot \sin(w \cdot t_i) = \{a_1\} \cdot \cos(w \cdot t_i) + \{-a_2\} \cdot \sin(w \cdot t_i); \tag{15}$$

$$A_{1,RMS} = \frac{A_1}{\sqrt{2}} = \sqrt{\frac{a_1^2 + a_2^2}{2}} \tag{16}$$

$$\phi_1 = \tan^{-1}\left(\frac{a_2}{a_1}\right) \tag{17}$$

More details on phasor computation are provided in the appendices (for continuous-time and discrete-time signals). In the case where the original signal contains harmonics, the phasor computed from (16) and (17) becomes the filtered phasor for the fundamental signal component. The magnitude of the aggregate phasor will feature oscillatory behavior because of the harmonics present. The phase angle of the aggregate phasor will feature the cumulative effects of the phase shifts of the individual harmonic contributions.

The phase angle at each instant (time $t = n{\cdot}Ts$), after the first cycle or period of samples, can be recursively calculated from the computed full-cycle-phasor. However, under unfaulted, normal system conditions, the phase angle computation from only one period may suffice. The phase angle error (PAE) can then be computed using (18).

$$\Delta\theta(t) = \theta_p(t) - \theta_{p\_est}(t) \quad (or, \quad \Delta\theta_{1-cycle} = \theta_{p\_1-cycle} - \theta_{p\_est\_1-cycle}) \tag{18}$$

5.3 Frequency Domain Comparison Methods

The frequency spectra of the estimated and uncorrected voltage signals are respectively compared against the spectrum of the ratio voltage reference. The respective signals are discrete sequences of finite lengths; thus, the *N*-Point Discrete Fourier Transform (*N*-DFT) [11] is used to generate the respective frequency spectra, where N represents the applied length of the sequence data. The *N*-DFT formula is shown in (19). Larger *N* values improve resolution in the frequency spectrum.

$$V[k] = \sum_{n=0}^{N-1} v[n] \cdot e^{-j2\pi nk/N}, \qquad 0 \le k < N \tag{19}$$

The difference between the estimated voltage or the uncorrected voltage and the ratio voltage reference generates an error signal. The energy in the error signal, with respect to either the estimated or uncorrected voltage, can be evaluated in the frequency spectrum using the DFT version of Parseval's Theorem [7, 9], as shown in (20).

$$error\_energy = \frac{1}{N} \cdot \sum_{k=0}^{N-1} |\Delta V[k]|^2 = \sum_{n=0}^{N-1} |\Delta v[n]|^2, \qquad 0 \le k < N; \quad 0 \le n < N \tag{20}$$

where *ΔV[k]* represents the error signal in the frequency domain and *Δv[n]* represents the error signal in the discrete-time domain. The error-energy formula in (20) can be directly related to the NRMSE (%) index shown earlier in (13) using the relationships in (21) and (22) – where 1/*D* is included as a matching or proportionality factor.

$$error\_energy = \frac{1}{N} \cdot \sum_{k=0}^{N-1} |\Delta V[k]|^2 = \sum_{n=0}^{N-1} |\Delta v[n]|^2 = \frac{1}{D} \cdot \left\{ \frac{(\varepsilon_{NRMSE}\%) \cdot \sqrt{N} \cdot M}{100} \right\}^2 \tag{21}$$

$$M = \max(v_{ratio}) - \min(v_{ratio}) \tag{22}$$

5.4 Results Presentation

Table 1 through Table 4 summarize the results. For brevity, only the plots relating to use-case scenario 3 are shown – that is, resistive load of 50 Ω and cable length of 0.16 miles (844.8 ft). For scenario 3, the time domain, filtered phasor domain and frequency domain plots are presented in Figs. 5 through 8 respectively.

It is important to note that VT resistive load values are typically high (e.g. 1000 Ω), representing low Volt-Ampere (VA) power consumption – which is generally true for electronic or microprocessor loads, as opposed to electromechanical loads. Therefore, reducing the resistive load draws higher inductive current through the instrumentation channel, causing phase and magnitude (or voltage-drop) errors. Increasing the channel cable length increases both the resistance and inductance properties of the channel, thereby also contributing to phase and magnitude errors. Therefore, generally, reducing the load resistance and/or increasing the cable length increases error generation in the instrumentation channel.

Table 1. Ratio error comparison (computed using instantaneous values)

BEFORE CORRECTION			AFTER CORRECTION			
Load (Ω)	*Cable Length (ft)*	*Ratio Error NRMSE(%)*	*Load (Ω)*	*Cable Length (ft)*	*Ratio Error NRMSE(%)*	*% Error Reduction*
50	52.8	**0.68**	50	52.8	**0.1**	85.29%
50	422.4	**0.91**	50	422.4	**0.12**	86.81%
50	844.8	**1.3**	50	844.8	**0.17**	86.92%

Table 2. Phase-angle error comparison computed using the filtered phasor for the fundamental (f_0) component.

BEFORE CORRECTION			AFTER CORRECTION			
Load (Ω)	*Cable Length (ft)*	*f_0 Phase Angle Error (deg)*	*Load (Ω)*	*Cable Length (ft)*	*f_0 Phase Angle Error (deg)*	*% Error Reduction*
50	52.8	**0.63**	50	52.8	**0.02**	96.83%
50	422.4	**0.67**	50	422.4	**0.02**	97.01%
50	844.8	**0.7**	50	844.8	**0.02**	97.14%

Table 3. Error signal energy (full sequence)

BEFORE CORRECTION			AFTER CORRECTION			
Load (Ω)	*Cable Length (ft)*	*Error Signal Energy*	*Load (Ω)*	*Cable Length (ft)*	*Error Signal Energy*	*% Error Reduction*
50	52.8	**21600**	50	52.8	**4.58E+03**	78.80%
50	422.4	**2.76E+05**	50	422.4	**8.77E+03**	96.82%
50	844.8	**9.32E+05**	50	844.8	**1.98E+04**	97.88%

Table 4. Error signal energy. Harmonic Band of $[-12, 12]$, to include the $(\pm)$ 1^{st}, 9^{th} & 11^{th}

BEFORE CORRECTION			AFTER CORRECTION			
Load (Ω)	*Cable Length (ft)*	*Error Signal Energy*	*Load (Ω)*	*Cable Length (ft)*	*Error Signal Energy*	*% Error Reduction*
50	52.8	**3.60E+04**	50	52.8	**7.60E+03**	78.89%
50	422.4	**4.61E+05**	50	422.4	**1.38E+04**	97.01%
50	844.8	**1.56E+06**	50	844.8	**3.03E+04**	98.06%

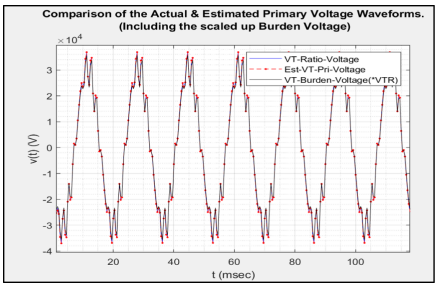

Fig. 5. (Zoom-In) instantaneous plots for use-case scenario 3.

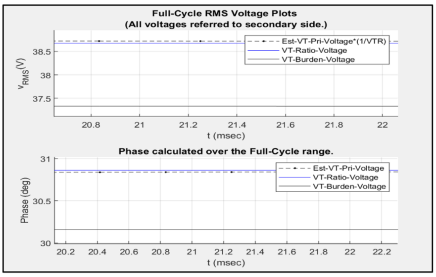

Fig. 6. (Zoom-In) fundamental RMS Ampl. & phase plot for use-case scenario 3.

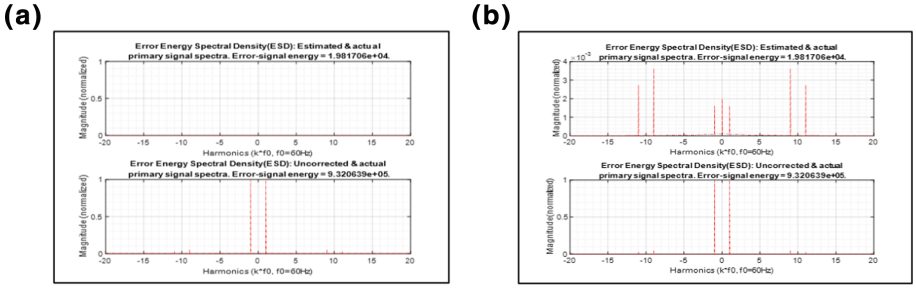

Fig. 7. (a) Full-Spectrum Error Signal ESDs, cross-normalized for easier correlation of energy levels across both plots. (Case 3), (b) (With zoom-in on top plot) Full-spectrum error signal ESDs, cross-normalized for easier correlation of energy levels across both plots. (Case 3)

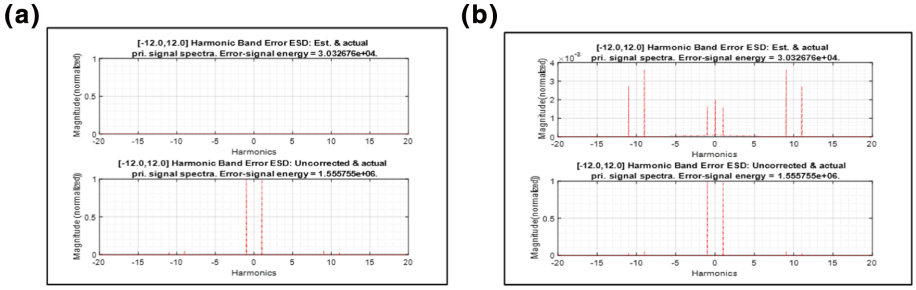

Fig. 8. (a) Error signal ESDs, only computed over the [−12,12] harmonic band, & cross-normalized for easier correlation of energy levels across both plots. (Case 3), (b) (With zoom-in on top plot) Error signal ESDs, only computed over the [−12,12] harmonic band, & cross-normalized for easier correlation of energy levels across both plots. (Case 3)

6 Observations and Conclusion

The results presented in Tables 1, 2, 3, and 4 both confirm and quantify the degrees of correction successfully accomplished by the method under evaluation. Note that in Table 2, the phase angle is computed from the filtered phasor and thus represents the angle of the fundamental frequency component (for either the uncorrected or estimated signals) – here, for each cable length, the error-correction algorithm produces a signal estimate with a fundamental phase angle (FPA) remaining at 99.94% of the FPA of the ratio voltage reference (RVR); while the FPA of the uncorrected voltage is respectively at 97.96%, 97.83% and 97.73% of the FPA of the RVR.

The frequency spectral analyses also confirm successful error correction outcomes by the method under evaluation. Figures 7, 8 show outcomes for the Simulation Use-case Scenario 3, simulating a 50 Ω VT resistive load with a channel cable length of 0.16 miles. Figs. 8a and b focus on a specified harmonic band, while Figs. 7a and b show the full spectrum. It can clearly be seen in Figs. 7 through 8 that the error signal energy spectral density (ESD) at the fundamental frequency is much lower after correction (top subplots) than before correction (bottom subplots) – the same positive observation is made for the 9th and 11th harmonics. Upon zooming in, as shown in Figs. 7b and 8b, it is worth noting that there is some signal energy at the 0^{th} harmonic in the error-signal spectrum after correction, not present before correction. This relatively insignificant but nonetheless present amount of energy at the 0^{th} harmonic (or 0-Hz) indicates the presence of a negligible but nonetheless present DC offset in the estimated time-domain voltage signal – which may result unavoidably from the applied estimation technique, or from minor improvement opportunities with the structure of the error-correction algorithm.

The paper has presented a new method that can correctly estimate the VT primary voltage that is corrupted by harmonic content. The presented method is also algorithmically structured for real-time implementation. Future work includes the development of the error-correction algorithm for the Coupled-Capacitor VT instrumentation channel, in addition to commencing efforts toward the hardware implementation of the method.

7 Appendices

A1: Full-Cycle Phasor Calculation: The Fourier series representation of any given cosine sinusoid is shown in (23), up to the m^{th} harmonic.

$$v(t) = A_1 \cdot \cos(w \cdot t + \phi_1) \; + \; A_2 \cdot \cos(2 \cdot w \cdot t + \phi_2) \; + \; \ldots. \; + A_m \cos(m \cdot w \cdot t + \phi_m) \tag{23}$$

The fundamental harmonic sinusoid at time t_i can be simplified using a trigonometry identity, as shown in (24). It can also be decomposed into a linear combination of phase-shifted sinusoids up to a K^{th} sinusoid, as shown in (25). Equation (25) is re-arranged and further simplified to (26). The expressions in the {.} brackets in (26) respectively represent quadrature constants, a_1 and a_2, shown in (27).

$$v(t_i) = A_1 \cdot \cos(w \cdot t_i + \phi_1) \; = \; \{A_1 \cdot \cos(\phi_1)\} \cdot \cos(w \cdot t_i) \; - \; \{A_1 \cdot \sin(\phi_1)\} \cdot \sin(w \cdot t_i) \tag{24}$$

$$
\begin{aligned}
v(t_i) &= A_1 \cdot \cos(w \cdot t_i + \phi_1) \\
&= A_{11} \cdot \cos(w \cdot t_i + \phi_{11}) \ + A_{12} \cdot \cos(w \cdot t_i + \phi_{12}) \ + \ ... \ + A_{1K} \cdot \cos(w \cdot t_i + \phi_{1K}) ; \\
&= A_{11} \cdot \{\cos(w \cdot t_i) \cdot \cos(\phi_{11}) \ - \ \sin(w \cdot t_i) \cdot \sin(\phi_{11}) \} \ + \ ... \\
&+ \ A_{1K} \cdot \{\cos(w \cdot t_i) \cdot \cos(\phi_{1K}) \ - \ \sin(w \cdot t_i) \cdot \sin(\phi_{1K}) \} \qquad (25)
\end{aligned}
$$

$$
= \{\sum_{J=1}^{K} A_{1K} \cdot \cos(\phi_{1K})\} \cdot \cos(w \cdot t_i) \ - \ \{\sum_{J=1}^{K} A_{1K} \cdot \sin(\phi_{1K})\} \cdot \sin(w \cdot t_i); \qquad (26)
$$

$$
\begin{aligned}
&= \{a_1\} \cdot \cos(w \cdot t_i) \ - \ \{a_2\} \cdot \sin(w \cdot t_i); \\
&= \{a_1\} \cdot \cos(w \cdot t_i) \ + \ \{-a_2\} \cdot \sin(w \cdot t_i); \qquad (27)
\end{aligned}
$$

The coefficients of Eqs. (27) and (24) can be respectively compared and mathematically operated upon to derive the phasor magnitude and angle, as shown in (28) through (32).

$$
a_1 = A_1 \cdot \cos(\phi_1) = \{\sum_{J=1}^{K} A_{1K} \cdot \cos(\phi_{1K})\} \qquad (28)
$$

$$
a_2 = A_1 \cdot \sin(\phi_1) = \{\sum_{J=1}^{K} A_{1K} \cdot \sin(\phi_{1K})\} \qquad (29)
$$

$$
A_1 = \sqrt{A_1^2 \cdot \{\cos^2(\phi_1) + \sin^2(\phi_1)\}} \ = \sqrt{a_1^2 \ + \ a_2^2} \qquad (30)
$$

$$
A_{1,RMS} = \frac{A_1}{\sqrt{2}} = \sqrt{\frac{a_1^2 \ + \ a_2^2}{2}} \qquad (31)
$$

$$
\phi_1 = \tan^{-1}\left(\frac{a_2}{a_1}\right) \qquad (32)
$$

Now, assume a sinusoidal waveform at the fundamental frequency, and uniformly sampled at N samples per period – where t_i in subsequent equations now means $i{\cdot}T_S$ or the i^{th} time interval, T_S. The phasor calculation begins by decomposing $v[i] = v(i{\cdot}T_S)$ into quadrature components A_i and B_i, and respectively summing these values over a period to obtain A and B – shown in (33) and (35). Applying (27), A and B can be respectively resolved and directly related to a_1 in (34) and a_2 in (36). Now, introducing two RMS quadrature parameters, P_1 and P_2, and respectively relating them with a_1 and a_2, as shown in (37) and (38), the full-cycle phasor can be calculated in (39) through (43), and shown to relate to the results in (30 and 31) through (32). The phasor is computed once after each cycle of the sampled signal.

$$
\begin{aligned}
A &= \sum_{i=1}^{N} v[i] \cdot \cos(w \cdot i \cdot T_S) \\
&= \{a_1\} \cdot \sum_{i=1}^{N} \cos^2(w \cdot i \cdot T_S) \ + \ \{-a_2\} \cdot \sum_{i=1}^{N} \sin(w \cdot i \cdot T_S) \cdot \cos(w \cdot i \cdot T_S);
\end{aligned}
$$

$$= \{a_1\} \cdot \sum_{i=1}^{N} \{\frac{1}{2} + \frac{\cos(2 \cdot w \cdot i \cdot T_S)}{2}\} \; + \; \{-a_2\} \cdot \sum_{i=1}^{N} \sin(w \cdot i \cdot T_S) \cdot \cos(w \cdot i \cdot T_S); \tag{33}$$

$$= \{a_1\} \cdot \sum_{i=1}^{N} \{\frac{1}{2}\} + \; 0 \; + \; \{-a_2\} \cdot 0 \; = \; a_1 \cdot \frac{N}{2}; \tag{34}$$

$$B = \sum_{i=1}^{N} v[i] \cdot \sin(w \cdot i \cdot T_S)$$

$$= \{a_1\} \cdot \sum_{i=1}^{N} \sin(w \cdot i \cdot T_S) \cdot \cos(w \cdot i \cdot T_S) \; + \; \{-a_2\} \cdot \sum_{i=1}^{N} \sin^2(w \cdot i \cdot T_S) \, ;$$

$$= \; \{a_1\} \cdot \sum_{i=1}^{N} \sin(w \cdot i \cdot T_S) \cdot \cos(w \cdot i \cdot T_S) \; + \; \{-a_2\} \cdot \sum_{i=1}^{N} \{ \frac{1}{2} - \frac{\cos(2 \cdot w \cdot i \cdot T_S)}{2} \} ; \tag{35}$$

$$= \{a_1\} \cdot 0 \; + \; \{-a_2\} \cdot \sum_{i=1}^{N} \{\frac{1}{2}\} \; = \; -a_2 \cdot \frac{N}{2}; \tag{36}$$

$$A = a_1 \cdot \frac{N}{2} \;\; \rightarrow \;\; a_1 = \frac{2 \cdot A}{N} = \sqrt{2} \cdot P_1 \tag{37}$$

$$B = -a_2 \cdot \frac{N}{2} \;\; \rightarrow \;\; a_2 = \frac{-2 \cdot B}{N} = \sqrt{2} \cdot P_2 \tag{38}$$

$$P_1 = \; \frac{a_1}{\sqrt{2}} = \frac{2 \cdot A}{\sqrt{2} \cdot N} = \sqrt{2} \cdot \frac{A}{N} \tag{39}$$

$$P_2 = \; \frac{a_2}{\sqrt{2}} = \frac{-2 \cdot B}{\sqrt{2} \cdot N} = (-1) \cdot \sqrt{2} \cdot \frac{B}{N} \tag{40}$$

$$P = P_1 + jP_2 \; = \cdot \frac{\sqrt{2}}{N} \cdot \{A - jB\} \tag{41}$$

$$|P| = \sqrt{P_1^2 + P_2^2} = \frac{\sqrt{2}}{N} \cdot \{\sqrt{A^2 + (-B)^2}\}$$

$$= \sqrt{\frac{a_1^2 \; + \; a_2^2}{2}} = \frac{A_1}{\sqrt{2}} = A_{1,\,RMS} \tag{42}$$

$$\phi_1 = \tan^{-1}(\frac{P_2}{P_1}) = \tan^{-1}\{ \; \frac{(-1) \cdot \sqrt{2} \cdot \frac{B}{N}}{\sqrt{2} \cdot \frac{A}{N}} \; \} = \tan^{-1}\{ \; \frac{-B}{A} \; \}$$

$$= \tan^{-1}\{ \; \frac{a_2}{a_1} \; \} \tag{43}$$

A2: Half-Cycle Phasor (Magnitude) Calculation: After each half cycle, (44) and (45) can be used to calculate the RMS value of the sampled sinusoid – where H represents half the number of samples per period or $N/2$; j iterates through every H^{th} set of samples, resulting in the calculation of the RMS value every half cycle.

$$i_{avg,\,j} = \frac{1}{H} \cdot \sum_{k=((j-1)\cdot H+1)}^{j\cdot H} |i_{sampled}[k]| \tag{44}$$

$$i_{sampled,\,RMS,\,j} = 0.9 \cdot i_{avg,\,j} \tag{45}$$

A3: Quarter-Cycle Phasor Calculation: After each quarter cycle, two quadrature samples are extracted from the sampled signal. Equations (46) through (48) are used to compute the phasor at system frequency.

$$s_1 = i_{sampled}[j] \tag{46}$$

$$s_2 == i_{sampled}[j - (\frac{N}{4} - 1)] \tag{47}$$

$$A_{1,RMS} = \frac{1}{\sqrt{2}} \cdot \sqrt{s_1^2 + s_2^2} \tag{48}$$

References

1. Izykowski, J., Kasztenny, B., Rosolowski, E., Saha, M.M., Hillstrom, B.: Dynamic compensation of capacitive voltage transformers. IEEE Trans. Power Deliv. **13**(1), 116–122 (1998)
2. Hamrita, T., Heck, B., Meliopoulos, S.: On-line correction of errors introduced by instrument transformers in transmission-level steady-state waveform measurements. IEEE Trans. Power Deliv. **15**(4), 1116–1120 (2000)
3. Sun, J., Wen, X., Lan, L., Li, X.: Steady-state error analysis and digital correction for capacitor voltage transformers. In: 2008 International Conference on Electrical Machines and Systems, Wuhan (2008)
4. Obikwelu, C., Meliopoulos, S.: VT instrumentation channel error correction using dynamic state estimation. In: 2021 North American Power Symposium (NAPS), Arizona (2021). (Accepted)
5. Obikwelu, C., Meliopoulos, S.: CT instrumentation channel error correction using dynamic state estimation. In: 2019 North American Power Symposium (NAPS), Wichita (2019)
6. Cokkinides, M.G., Stefopoulos, G.: Quadratic integration method. In: Proceeding of International Power System Transients conference, Montreal (2005)
7. Moon, T., Stirling, W.: Mathematical Methods and Algorithms for Signal Processing. Prentice Hall (2000)
8. Kezunovic, M., Meliopoulos, S., Venkatasubramanian, V., Vittal, V.: Application of Time-Synchronized Measurements in Power System Transmission Networks. Springer, Heidelberg (2014). https://doi.org/10.1007/978-3-319-06218-1
9. Bracewell, R.N., Bracewell, R.N.: The Fourier Transform and its Applications. McGraw-Hill, New York (1986)

10. https://www.ap-concepts.com/win_igs.htm. Advanced Power Concepts
11. Rebizant, W., Szafran, J., Wiszniewski, A.: Digital Signal Processing in Power System Protection and Control. Springer-Verlag, London (2011). https://doi.org/10.1007/978-0-85729-802-7
12. Obikwelu, C., Meliopoulos, S.: CT saturation error correction within merging units using dynamic state estimation. In: 2020 IEEE 3rd International Conference on Renewable Energy and Power Engineering (REPE), Edmonton, Canada, October 2020